PNAS
www.pnas.org

Supplementary Information for

Configurational Entropy of Basaltic Melts in Earth's Mantle

Sung Keun Lee[1*], Jed L. Mosenfelder[2], Sun Young Park[1], A Chim Lee[1], and Paul D. Asimow[3]

[1]*School of Earth and Environmental Sciences, Seoul National University, Seoul, 08826 Korea*

[2]*Department of Earth Sciences, University of Minnesota, Minneapolis, MN, 55415 USA*

[3]*Division of Geological & Planetary Sciences, California Institute of Technology, Pasadena, CA 91125 USA*

*Correspondence to S.K.L (Email: sungklee@snu.ac.kr)

This PDF file includes:

Supplementary text
Figs. S1 to S3
Table S1 to S3
References for SI reference citations

www.pnas.org/cgi/doi/10.1073/pnas.2014519117

Supplementary Information (SI) Text

S1. The degree of polymerization in silicate glasses:

The trend in the partition coefficients of elements between basaltic melts and coexisting crystalline phases in the upper mantle may originate from structural changes, such as the formation of highly coordinated framework cations and changes in the degree of melt polymerization (1). ^{17}O NMR allows us to estimate the fractions of the oxygen atoms in a glass that are bonded to various cations. As Si and Al are network-forming cations, oxygens in groups such as $^{[4]}$Si-O-$^{[4]}$Si, $^{[4]}$Si-O-$^{[5,6]}$Si, Si-O-$^{[4]}$Al, $^{[4]}$Si-O-$^{[5,6]}$Al and $^{[4]}$Al-O-$^{[4]}$Al are called bridging oxygens (BO), whereas oxygens in groups such as {Ca, Mg}-O-$^{[4]}$Si are nonbridging oxygens (NBO). The degree of polymerization of a silicate composition is often parameterized by the mole fraction of NBO (X_{NBO}, the number of NBO per total oxygens) that can be directly estimated from multi nuclear NMR. Furthermore, it has also been parameterized by the number of NBO per tetrahedrally-coordinated cation, NBO/T [that can vary from 0 (fully polymerized) to 4 (fully depolymerized)]. The estimated X_{NBO} and NBO/T of the $Di_{64}An_3$ glasses at 1 atm are ~0.38 and ~1, respectively. Therefore, the model basaltic glasses are partially depolymerized and have an intermediate degree of network polymerization.

S2. Structure of multi-component silicate melts and glasses upon compression: Utility and limitation of scattering techniques and solid-state NMR:

Below we briefly summarize the known utility and limitation of diverse conventional scattering and spectroscopic experimental techniques and solid-state NMR (a main technique of the current study) of multi-component aluminosilicate glasses at high pressure. More detailed information is available in the original manuscripts and references therein.

Scattering and spectroscopic studies. A number of pioneering, experimental scattering (both X-ray and neutron scattering) studies provide direct insights into the pressure-induced evolution of the short-to-medium range atomic configurations in silicate and oxide glasses and melts under compression [e.g., (2-18) and references therein]. Applications of the scattering techniques have mostly been focused on glasses with relatively simple compositions because of overlap among multiple binary correlation functions within relatively narrow ranges of radial distance in multi-component systems: at ambient pressure, it is still challenging to obtain model-free coordination numbers of Si and Al in multi-component aluminosilicate glasses at even with collections of structure factors up to 40 $Å^{-1}$ [e.g., (19)]. This is partly because the scattering factors for these low-Z elements (e.g., Si and Al) as well as their difference are rather small. At high pressure, the pressure-induced transitions in coordination environments in silicate glasses under densification can be more challenging, mostly because of the somewhat limited scattering vector under elevated pressure conditions, constrained by the geometry and sample confining environments within high-pressure devices.

It is also not trivial to unambiguously yield model-free structures of multi-component oxide glasses at high pressure through vibrational spectroscopy (i.e., Raman and IR), where overlaps among broad vibrational modes are inherent. Although element-specific techniques like X-ray absorption and inelastic X-ray Raman spectroscopy can be effective, similar broadening in the overall spectral features is observed with increasing number of oxide components at high pressure. Therefore, the challenges of yielding unique structural information about multi-component oxide glasses under compression remain [see (13, 20) and references therein].

Solid-state NMR. 1D MAS (magic angle spinning) and 2D 3Q (triple quantum) MAS NMR on diverse NMR-active, spin-1/2 (e.g., ^{29}Si) and quadrupolar nuclides (e.g., ^{27}Al, ^{17}O, and ^{23}Na) have provided pressure-induced changes in atomic structures around framework cations (e.g., Si and Al), non-framework cations (e.g., Na, Ca), and certain types of oxygens (e.g., bridging and non-bridging oxygen, S2) in oxide glasses [(1, 21-25) and references therein]. These NMR studies enable quantification of the degree of polymerization (1, 23) and short-range structural parameters in multicomponent aluminosilicate glasses at low

pressure conditions [e.g., (26, 27)]. Particularly, the detailed 1 atm structure of multi-component $Di_{64}An_{36}$ [diopside ($CaMgSi_2O_6$)–anorthite ($CaAlSi_2O_8$) eutectic composition] glass was explored using solid-state NMR [see (28, 29) and references therein]. The NMR study also presents evidence of a small percentage increase in the fraction of $^{[5]}Al$ in shock-compressed $Di_{64}An_{36}$ glass (30). Despite previous efforts, the NMR peaks for geologically relevant Mg-bearing aluminosilicate glasses are difficult to analyze in part because of the larger field strength of Mg^{2+}, which leads to significant peak-broadening in the NMR spectra (31). Furthermore, applications of the NMR have mainly been limited to *iron-free* oxide glasses because interactions between nuclear spins and unpaired electrons in paramagnetic elements, including iron result in a decreases in NMR signal and a significant broadening in NMR spectrum (32). Broadening in the NMR spectra for oxide glasses at high pressure conditions also becomes prevalent with increasing number of oxide components, making it difficult to yield unique structural insights. The pronounced heterogeneous spectral broadening stems from a pressure-induced increase in diverse aspects of configurational disorder in amorphous oxides, such as the formation of highly coordinated cation and anion species, the enhanced mixing among these structural units, and the broader bond-angle and length distributions. Therefore, the effect of pressure on the detailed structures of multi-component mafic melt at its formation depth has not been fully understood.

S3. Composition of synthetic model basaltic glasses:

The effect of melt composition on Al coordination environment of multi-component basaltic glasses was explored (Figure 1, bottom-left). Here, the chemical compositions of the glasses were from those of the KLB-1 basaltic melts with varying formation depth up to 3 GPa (33). Because of the pronounced paramagnetic effect (due to the strong coupling between nuclear spins and unpaired electrons in iron), signal intensity decreases noticeably with increasing iron content. Therefore, we replaced FeO and Fe_2O_3 components from the composition of KLB-1 basaltic glasses by MgO and Al_2O_3, respectively. The Mg:Al ratio is from the reported Fe^{2+}:Fe^{3+} ratio of iron in MORB glasses (29, 34) (Table S2). While further experimental study is necessary to confirm the effect of Mg on the Al coordination environments at high pressure, Mg-rich aluminosilicate glasses is difficult to synthesize at high pressure because of the formation of quench crystals and the high melting temperature at an elevated pressure condition.

S4. Structural difference in the silicate liquids and the quenched glasses:

The structures of model basaltic glasses quenched from melts at high pressure preserve those of compressed liquids that are super cooled below its melting temperature (T_m), but are frozen at the glass transition temperature (T_g) (35). Because T_m is higher than T_g, the glass structure is not identical to that at T_m (see S11 for detailed discussion).

S5. Shearing of ^{27}Al 3QMAS NMR spectra for the model basaltic glasses:

Figure S1 shows the ^{27}Al 3QMAS NMR spectra for the model basaltic glasses without additional shearing (Figure S1. A) and with an additional shearing factor to align the Al sites to be parallel to the MAS-dimension (y-axis) (Figure S1. B).

S6. ^{29}Si NMR spectra for the model basaltic glasses quenched from melts at high pressure:

Figure S2 shows the ^{29}Si NMR spectra for the model basaltic glasses at 1 atm and 5 GPa. Expected peak positions for $^{[5,6]}$Si species are ~-140 ppm ($^{[5]}$Si) and ~-190 ppm ($^{[6]}$Si), respectively (36, 37). These features are not detected in the ^{29}Si MAS NMR spectra of the glass at 5 GPa, so the total decrease in NBO is solely due to an increase in $^{[5,6]}$Al in the model basaltic melts up to 5 GPa.

S7. The extent of $^{[4,5,6]}$Al - $^{[4]}$Si distribution and densification mechanisms of basaltic liquids up to 5 GPa:

The degree of Al avoidance (Q) linearly decreases with increasing cation field strength from ~0.85 for Ca-aluminosilicate glasses (i.e., Q_{Ca}) to ~0.65 (Q_{Mg}) for Mg aluminosilicate glasses (31). Considering the Ca/(Ca+Mg) (X_{Ca}=0.61) ratio in the model basaltic glasses, the average Q value in the model basalt is expected to be ~0.77 [=Q_{Ca}* X_{Ca}+ Q_{Mg}* X_{Mg}]. The pressure-induced coordination transformation is responsible for the overall densification. The following scheme has been used to describe the formation of $^{[5,6]}$Al:

$^{[4]}$Si-O-$^{[4]}$Al + (Ca, Mg)-O-$^{[4]}$Si = $^{[4]}$Si-O-$^{[5]}$Al-O-$^{[4]}$Si···Ca*-Mg* (S1.1)

$^{[4]}$Si-O-$^{[5]}$Al + (Ca, Mg)-O-$^{[4]}$Si = $^{[4]}$Si-O-$^{[6]}$Al-O-$^{[4]}$Si···Ca*-Mg* (S1.2)

Ca^{2+} and Mg^{2+} play the roles of network-modifying cations in basaltic melts at 1 atm (forming Si-NBO). In contrast, as shown in the schemes above, these cations tend to balance the negative charge of the bridging oxygen [$^{[4]}$Si-O-$^{[5]}$Al-O-$^{[4]}$Si] formed at the expense of NBO with increasing pressure and thus tend to play a role of charge-balancing cations (shown with asterisks).

S8. Calculation of configurational entropy (S_{conf}) of basaltic liquids at ambient and high pressure:

Choice of mixing units for calculation of S_{conf}. The configurational entropy (S_{conf}) refers to the degree of disorder that is estimated from the pressure-induced changes in oxygen cluster populations resulting from the formation of different Al-coordination environments. S_{conf} in the melts at high pressure may be calculated by considering the mixing of oxygen clusters (1) such that:

$$S_{conf}(P) = -R\left\{\sum_i \left[X^i_{NBO}(P)\ln X^i_{NBO}(P)\right] + \sum_i \left[X^i_{BO}(P)\ln X^i_{BO}(P)\right]\right\} \quad \text{(S2)}$$

where X^i_{NBO} and X^i_{BO} are the mole fractions of NBO and BO clusters. Here, a single type of NBO ({Ca, Mg}-O-Si) cluster and four distinct types of BO ([4]Si–O–[4]Si, [4]Si–O–[4]Al, [4]Si–O–[5,6]Al, and [4]Al–O–[4]Al) clusters are taken into consideration. The calculated S_{conf} tends to increase with increasing pressure and then to decrease with further increase in pressure (Figure 4 and Figure S3). Below the pressure at which the maximum number of configurations is attained, the formation of highly coordinated Al and consequent rearrangement in oxygen configurations results in an increase in S_{conf}. This structural change is similar to an addition of a new chemical component in the melts, which increases S_{conf}. The increase in S_{conf} suggests that the flexibility of the melt network increases with pressure; the pronounced diversity in oxygen-site configurations and the formation of highly coordinated Al is expected to soften the mechanical strength of the network. The entropy factor is expected to decrease with further increases in the pressure, as the structural change no longer leads to configurational diversity in the networks.

S_{conf} beyond 5 GPa. It is not trivial to estimate S_{conf} beyond 5 GPa where NMR data for coordination states in the model basaltic glasses are not available. The formation of highly coordinated Si (e.g., [5,6]Si) in aluminosilicate melts is reported to be prevalent at much higher pressure (18, 38, 39). Therefore, [4]Si–O–[5,6]Si cluster is not taken into consideration explicitly in the current study, while the formation of [5,6]Si at higher pressure may increase the S_{conf}. The estimation of S_{conf} at higher pressure using the current set of mixing units would mean that highly coordinated species [5,6](Al, Si) act as a single mixing unit. Therefore, the S_{conf} above 5 GPa can be somewhat underestimated. Nevertheless, the distribution of [4]Si–O–[5,6](Si,Al) in the glass network is uniquely constrained by the distribution [4]Si-O-[4]Al, [4]Si-O-[4]Si, and NBO species**.** Distinguishing all the highly coordinated species and randomizing the distribution of the species would certainly overestimate S_{conf}. As the S_{conf} depends on the choice of the clusters, the current modeling above 5 GPa provides a qualitative guide to anomalous pressure-induced changes in melt properties.

S9. Quantification of oxygen species and the effect of X_{NBO} on S_{conf}:

While the ^{17}O NMR spectra for the model basaltic glasses at 1 atm and high pressure qualitatively confirm the formation of $^{[4]}$Si-O-$^{[5]}$Al, the absence of a Si-O-$^{[5,6]}$Si peak at high pressure, and the overall decrease in NBO fraction (Figure 2), overlap among peaks in the ^{17}O 3QMAS NMR spectra makes it difficult to directly and completely estimate all the oxygen species fractions at high pressure from the data alone. Despite the difficulty, the fractions of the NBO and each BO species can be calculated quite precisely at 1 atm from the combination of constraints from ^{27}Al NMR (Figure 1) — which yield robust estimates of the fractions of $^{[4,5,6]}$Al —with a numerical simulation based on statistical thermodynamic modeling of oxygen species at constant Q value of 0.77 (40). At high pressure, because the changes in oxygen configurations with pressure stem solely from the formation of $^{[5,6]}$Al, the NBO and BO fractions at elevated pressure can then be directly estimated: approximately, the reduction in 1 mole of NBO and Si-O-$^{[4]}$Al corresponds to the formation of 2 mole of Si-O-$^{[5,6]}$Al species. Uncertainly in oxygen site fraction results mostly from uncertainty in the $^{[4,5,6]}$Al species fractions and from variation of Q values. The estimated uncertainty in oxygen species in the model basaltic glass of ±3-4% leads to an uncertainty in the calculated S_{conf} value of ±0.2 J/K.

X_{NBO} at higher pressure conditions beyond 5 GPa. As the direct experimental X_{NBO} is available only up to 5 GPa, the data beyond 5 GPa are extrapolated from the data up to 5 GPa (Figure 4). It has been previously shown that the pressure-induced structural transitions, including X_{NBO} can be described as follows (1, 41):

$$X_{NBO}(P) = 1 - \exp[(P/P_{X_{NBO=0.5}} - 1)/\alpha] \quad \text{(S3)}$$

where α is a constant describing the degree of network rigidity upon compression and $P_{X_{NBO=0.5}}$ is the pressure where the X_{NBO} reaches 50% of the value at 1 atm (1, 41). Despite its utility, Eq. S3 may not correctly describe the pronounced distribution of structural units (i.e., coordination environments) in oxides glasses and melts and the smaller $[\partial X_{NBO}/\partial P]_T$ at higher pressure (i.e., change in X_{NBO} becomes more difficult with increasing pressure if X_{NBO}<0.5). Rather, these characteristics in X_{NBO} and pressure-induced structural transitions in glasses can be better described with the following equation based on the error function (42, 43):

$$X_{NBO}(P) = -\mathrm{Erf}[(P/P_{X_{NBO=0.5}} - 1)/\beta]/2 + 0.5 \quad \text{(S4)}$$

where β is a constant similar to α, quantifying the network rigidity during pressurization. While the calculated patterns (using Eq. S3 and S4) are similar up to X_{NBO}=0.5, the error function is more suitable to describe the pressure-induced transitions beyond X_{NBO}<0.5. Figure S3 shows the estimated X_{NBO} (blue line) and the corresponding $\overline{S}_{conf}$ (red line) with

varying pressure. Those with varying β [from 0.62 (thick dashed line) to 1 (thin dashed line)] demonstrate that a larger X_{NBO} at a given pressure leads to a smaller $\bar{S}_{conf}$ and $\bar{S}_{conf}*V$. We note again that the estimated X_{NBO} above 5 GPa is subject to a moderate degree of uncertainty as the experimental confirmation of the trend in X_{NBO} at higher pressure remains.

S10. Molar volume of basaltic glasses under pressure:

Figure S3 shows normalized volume of diverse basaltic glasses and melts from *in situ* high-pressure measurements and *ab initio* calculations. Of course, all studies find that molar volume decreases with increasing pressure, but there are differences apparent among compositions and among measurement techniques. Whereas the origin of the systematic variation (and the effect of composition) is beyond the scope of the current manuscript, there is indeed non-negligible dispersion in the reported densities of the glasses and melts (44). For example, the estimated molar volume of CRB estimated from x-ray absorption is smaller than that from interferometry by up to ~ 15%. This indicates a moderate degree of uncertainty in the molar volume of the glasses with varying pressure. In the current study, molar volumes of $Di_{64}An_{36}$ melts (45) and BCR-2 glasses (44) were selected as models to account for pressure-induced mechanical properties. At the level of a conceptual model, the selection of only two compositions is justified because differences among compositions are in fact comparable to uncertainties due to experiment method. Future studies of the effect of composition remain. As demonstrated in Figure S5, the resulting trend for $\bar{S}_{conf}*\bar{V}$ varies depending on the pressure-induced changes in $\bar{V}$.

S11. Cation coordination environments in the glasses and the corresponding liquids at high pressure.

While there is, indeed, a minor structural difference between liquids and glasses, previous experimental studies confirm that the short-range structures, including the cation coordination environment, of liquids and of glass analogs at high pressure may not differ significantly (24, 25). As this is not the focus of the current study, we only provide brief discussion of the structural differences between glasses and melts. As for the glasses with simpler compositions, theoretical calculations indicated that the cation coordination environments for GeO_2 and SiO_2 glasses and the corresponding liquids are almost identical up to ~ 15 GPa (46). It has been shown that the Al coordination environment of amorphous (and thus glassy) Al_2O_3 is almost identical to the corresponding liquids at 1 atm [e.g., (47)]. The effect of temperature (from 3000 K to 6000 K) on the Al coordination number for the Al_2O_3 liquid is reported to be negligible (48). The average Si coordination number of the $MgSiO_3$ glasses is only slightly larger than that of the liquids at low pressure conditions (39,

49). Whereas the pressure is much higher, our recent *ab initio* calculations of $MgSiO_3$ glass and melts at 131 GPa shows that average Si coordination number does not change significantly (~6.06 at 3000 K to ~6.09 at 6000 K), while the dispersion of the Si coordination states may increase (50). The structural differences between the multi-component liquids and glass analogs at high temperature and pressure remain to be explored. Detailed high-resolution NMR studies showed that the fractions of highly coordinated Al slightly increases with increasing fictive temperature (51). We believe that current NMR methods provide a unique window through which to study the structures of multi-component super-cooled liquids at the glass transition temperature (e.g., detailed Al and Si coordination states). The fractions of $^{[5,6]}$Al may slightly increase at higher temperature, where the extent of configurational disorder is likely to be more pronounced. Taking this into consideration, more diverse structural units at high temperature conditions lead to an increase in S_{config}.]

S12. Structural origins of the mechanical weakening and transport properties of oxides glasses under compression:

In the earlier pioneering studies, the weakening of the mechanical properties of diverse oxide glasses with increasing pressure was observed (44, 52). The degree of melt polymerization (a fixed NBO/T) and the rotational degree of freedom play important roles in the overall weakening of the mechanical properties. Similarly, Liu and colleagues report the change in the elastic properties of glasses and propose that the changes are due to the pressure-induced changes in the void space (i.e., free volume) (53). Despite the progress, the structural origin of this phenomenon has remained to be explored: the structural data (i.e., independent Al, Si coordination numbers and the pressure-induced changes in the degree of melt polymerization from NBO and BO environments) for the multi-component silicate glasses are difficult to retrieve at ambient and high pressures. Only solid-state NMR provides unambiguous Al and Si coordination environments in multi-component silicate glasses at high pressure. In the current study, based on the unique structural data that we acquired, we found the link between configurational entropy and mechanic properties, providing a novel conceptual framework that is based on an unprecedented high-resolution structural measurement. Specifically, the current model of the scaled entropy with density provides a *qualitative* framework based on atomistic constraints) with which the elastic constants and the seismic wave velocity of the glasses (and potential melts) can be understood. We show that the NBO fraction is not constant, but decreases with increasing pressure by forming highly coordinated Al, which we use to calculate the S_{conf}. Therefore, in addition to Clark et al.'s experimental breakthrough (44, 52), we provide novel conceptual breakthroughs based on the measurement of the true structural data that we acquired using solid state NMR. We also found that our S_{conf} should be well correlated with the rotational

degree of freedom that is inherent in the glass structures and the free volume (as shown in Figure 3).

We also note that in a recent molecular dynamics simulation of SiO_2 glass (54), a decrease in the macroscopic bulk modulus results from an increase in number of micro-jumps. While the dynamic jump event cannot be specified from the static structural information provided in our manuscript, the non-linear change in the number of micro-jumps from the theoretical study can be inferred from the pressure-induced changes in S_{conf}/density: the number of micro-jumps may increase with the degree of network flexibility and the number of configurational available to jump events, and therefore, S_{conf}. It may also decrease with increasing density of network. Therefore, the maximum of S_{conf}/density is expected to be positively correlated to the number of micro-jumps.

As for the diffusivity of metal cation in silicate glasses, it has been shown that that the Al diffusion maximum is related to an increase in the Al coordination number (55). An increase in configurational entropy (S_{conf}) has been linked to a decrease in melt viscosity: S_{conf} (without normalization with its density) was used to describe the melt viscosity at high pressure (56-59). An excellent review chapter on this issue is also available [e.g., (60)].

S13. Insights into the effects of pressure on trace element compatibility in basaltic melts:

While the current proposal takes the S_{conf} and melt volume into consideration to account for the non-linear variation of pressure-induced changes in the mechanical properties of glasses, the results can also provide qualitative insights into other properties, including trace element compatibility. For example, the solubility of a high field-strength (charge/cation radius) cation (HFSC) tends to increase with decreasing melt SiO_2 content [See (61) and references therein]. This trend suggests that the HFSCs may have a strong affinity with nonbridging oxygen. Therefore, the decrease in NBO content that we have documented would make it more difficult to incorporate these elements into melts at high pressure (1). The current result also suggests that the observed changes in partition coefficients of elements between basaltic melts and coexisting crystalline phases in the upper part of the mantle may originate from the reduction in NBO and/or the formation of highly coordinated framework cations.

The pressure-induced changes in the atomic configurations in silicate melts allow us to speculate on the atomistic origin of the anomalous U/Pb ratio of mantle-derived rocks. As U decays into Pb through multiple decaying processes, providing that the U content of the primitive mantle has been constant over ~4.5 billion years, the U/Pb ratio of mantle-derived rock is expected to decrease over geologic time. Furthermore, U is more incompatible than Pb below 2 GPa (62), so more U (compared with Pb) is expected to be enriched in melts, and

the residual mantle is expected to lose U during partial melting, resulting in a decrease in U/Pb over time. This ratio is opposite that of observed mantle and crustal rocks and is known as the Pb paradox (62). The anomalous U/Pb ratio has been attributed to the partitioning of Pb into the core, as Pb is both a chalcophile and a siderophile element, to the volatile nature of Pb and, thus, the potential loss of Pb during initial stages of planetary accretion [see (62) and references therein], and to the preferential incorporation of Pb into continental crust due to its mobility in subduction zone fluids (63). Alternatively, the current study shows that the relative compatibility of these elements in silicate melts at high pressure may differ significantly from compared to 1 atm (and relatively low-pressure conditions). This difference may account for the increased U in the silicate melts at high pressure. Indeed, based on experimental partitioning between Ca (and Mg)-perovskite and melt, U is more compatible than Pb (by 1-1.5 order of magnitude) at ~25 GPa [ref.(64)], indicating a drastic reversal of compatibility at higher pressure.

S14. Effect of temperature and volatile contents on the structure of multi-component glasses:

The structures of model basaltic glasses quenched from melts at high pressure preserve those of compressed liquids that are super cooled below its melting temperature (T_m), but are frozen at the glass transition temperature (T_g) (35). Because T_m is higher than T_g, the glass structure is not identical to that at T_m. Furthermore, upon quenching, the pressure conditions in the assembly can be lower than the desired pressure. Because we explore iron-free model basaltic glasses in the nominal absence of fluids (H_2O and CO_2), their effects on the structures of melts remain to be explored.

S15. Pressure uncertainty for high pressure synthesis via melt-quenching:

Upon quenching, the pressure conditions in the assembly can be lower than the desired pressure (26, 65). An earlier study on melting of aluminosilicates reported deviation from the desired pressure in multi-anvil apparatus (65); with increasing temperature at constant load designed to reach 6 GPa, the pressure increased up to ~7 GPa, and upon quenching, pressure can decrease up to ~4.5 GPa. Similar pressure drop has been suggested to account for the observed differences in the Al fractions estimated at near the glass transition temperature and those quenched from melts (26). Currently, because of differences in the assemblies, it is difficult to estimate the potential pressure drop quantitatively. We also note that the pressure drop in these earlier studies is based to a degree on the extrapolated fictive temperature at low pressure conditions. However, it is not clear whether the fictive temperature continues to decrease up to 5 GPa.

S16. Glass quenched from melts at high pressure *vs.* glass annealed near T_g at high pressure:

Recent studies of silicate glasses at high pressure near the glass transition temperature (T_g) revealed the structures of glasses that may not be accessible to typical melt-quench methods, such as Mg-rich silicate glasses and/or glasses with high melting temperature [e.g., (66)]. We note that the structural states of these glasses may not be clear due to temperature gradient within the assembly and uncertainty in T_g: the structure may represent a metastable snapshot of one of the plastically deformed states. The structures are also manifesting the diverse temperature variations within the sample. In contrast, the physical states of quenched glasses from liquids are clearly defined by the melt-quench and, thus, the process variable T_g. The glasses quenched from melts may not be subject to a structural heterogeneity.

SI Tables

Table S1. Fractions and NMR parameters [center of gravity, isotropic chemical shift (δ_{iso}^{CS}), quadrupolar coupling constant (C_q)] of Al sites obtained from ^{27}Al 3QMAS and MAS NMR spectra for (CMAS) glasses quenched at 1 atm and 5 GPa.

	Pressure (GPa)	Center of gravity (ppm)		δ_{iso}^{CS} (ppm)	C_q (MHz) (η = 0.5)*	Calibrated intensity (%)	MAS
		MAS dimension	Isotropic dimension				
$^{[4]}$Al	0	42.3±1.5	-42.0±1.5	63.9±1.5	6.0±0.5	97±2	97±2
	3	43.3±1.5	-42.4±1.5	64.7±1.5	6.0±0.5	74±3	76±3
	5	42.9±1.5	-42.7±1.5	64.9±1.5	6.1±0.5	61±3	60±3
$^{[5]}$Al	0	21.5±2.5	-21.1±2.5	32.2±1.5	4.2±0.5	4±2	3±2
	3	16.9±2.5	-21.5±2.5	30.9±1.5	4.8±0.5	18±2	15±2
	5	14.4±2.5	-22.3±2.5	30.9±1.5	5.3±0.5	23±2	24±3
$^{[6]}$Al	0	-	-	-	-	-	-
	3	-7.4±2.5	-2.7±2.5	0.3±1.5	3.6±0.5	8±2	8±2
	5	-9.9±2.5	-4.1±2.5	1.0±1.5	4.3±0.5	16±3	16±2

[a] Normalized to that of $^{[4]}$Al site.

*here asymmetry parameter of 0.5 is assumed.

Table S2. Nominal composition and ICP analysis of model (Fe-free) KLB-1 basaltic glasses. X_{MgO} is the mole fraction of MgO among non-framework cations [X_{MgO}=MgO/(CaO + MgO + Na_2O + K_2O)]. The table is from our previous report on these basaltic glasses (29).

Composition (mol%)	X_{MgO} 0.47	0.56	0.65
SiO_2	54.4	49.8	46.3
TiO_2	0.7	0.4	0.3
Al_2O_3	12.3	9.5	8.1
MgO	15.2	22.5	29.7
CaO	12.4	16	14.7
Na_2O	4.7	1.6	0.8
K_2O	0.2	0.1	0.1

Composition (mol%)	Nominal composition X_{MgO} 0.47	0.56	0.65	ICP analysis* X_{MgO} 0.47	0.56	0.65
TiO_2	1.5	0.8	0.6	1.6	1.0	1.0
Al_2O_3	27.0	19.0	15.1	23.5	16.7	13.3
MgO	33.4	44.9	55.2	34.9	47.0	57.9
CaO	27.3	31.9	27.4	28.9	31.9	26.2
Na_2O	10.3	3.2	1.5	10.6	3.2	1.4
K_2O	0.4	0.2	0.2	0.5	0.3	0.2

*SiO_2 in the glasses was removed by reacting with hydrofluoric acid for the ICP analysis.

Table S3. Compositions of diopside-anorthite eutectic ($Di_{64}An_{36}$), Icelandic basalt (BIR-1G), and Columbia River basalt (BCR-2G) glasses in wt%.

Sample	Composition (wt%)												Ref.*
	SiO_2	Al_2O_3	CaO	MgO	$FeO+Fe_2O_3$	Na_2O	K_2O	MnO	P_2O_5	TiO_2	H_2O	Total	
$Di_{64}An_{36}$	50.33	15.37	23.49	10.80								100	Current study
BIR-1G†	47.96	15.50	13.30	9.70	11.30	1.82	0.03	0.18	0.02	0.96		99.87	(1)
BCR-2G†	54.10	13.50	7.12	3.59	13.80	3.16	1.79		0.35	2.26	0.35	100.02	(2)

* (1) Liu et al. (2014) (53) (2) Clark et al. (2016) (44)

SI Figures

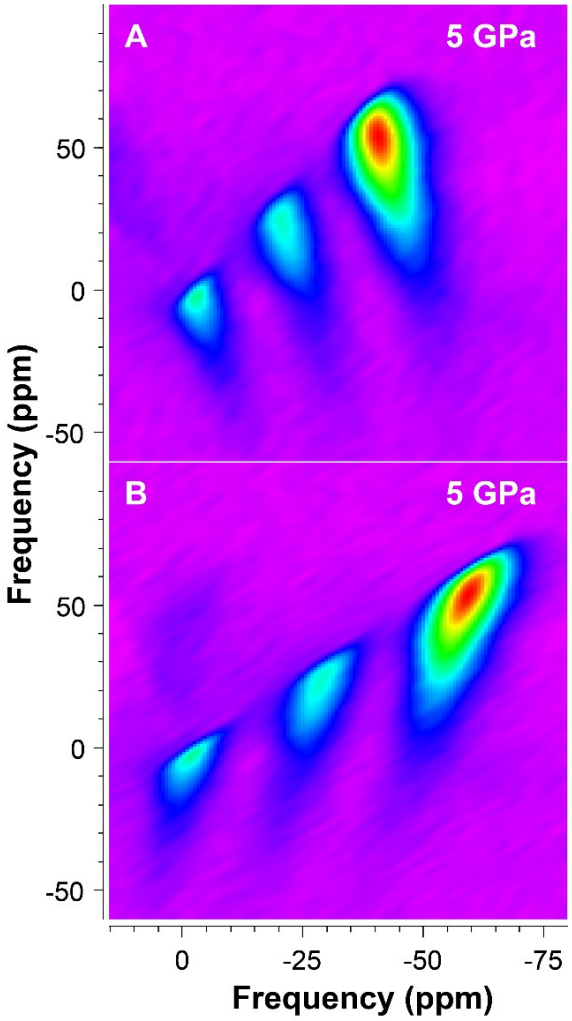

Figure S1 | 2-dimensional ^{27}Al 3QMAS NMR spectra for the model basaltic glasses. a. ^{27}Al 3QMAS NMR spectra for the model CMAS glasses quenched from melts 5 GPa (identical to figure 1, top). **b.** The spectrum in A was sheared (rotated) in such a way that the projection (into the x-axis) provides better-resolved Al sites with Gaussian peak shapes (Figure 1, bottom right). This increased resolution allowed for robust quantification of each Al site fraction. In the spectrum shown in A, Al sites in the total isotropic projection overlap, and the peak shape cannot be described with a single Gaussian function.

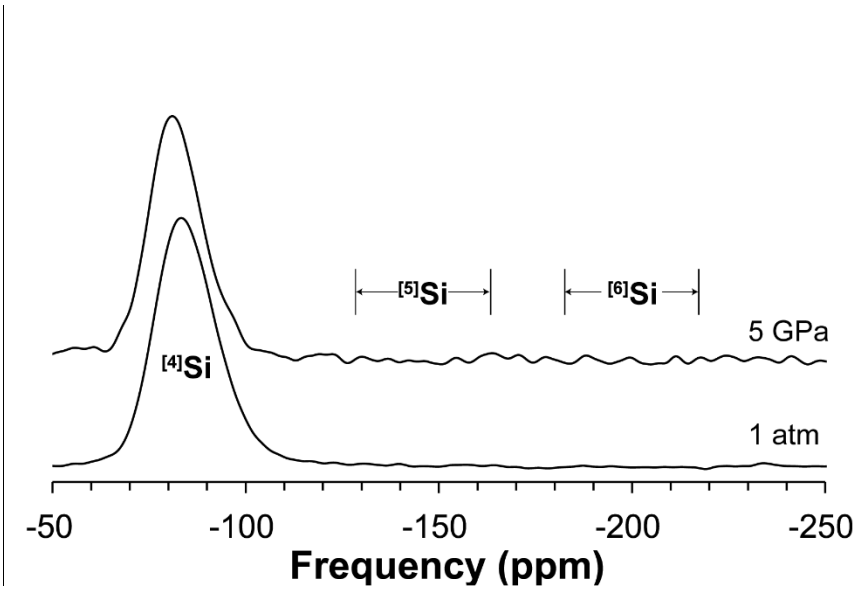

Figure S2 | ^{29}Si MAS NMR spectra for model basaltic glasses quenched from melts at 1 atm and 5 GPa.

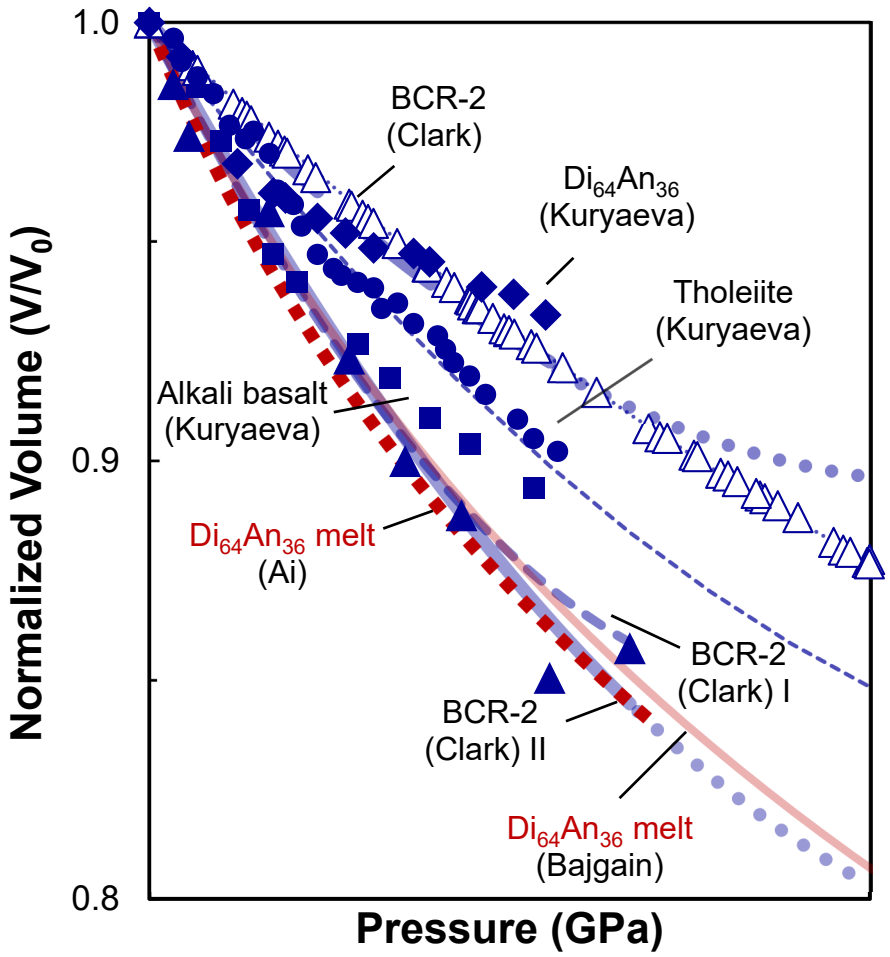

Figure S3| Effect of pressure on the normalized volume ($\overline{V}$) of diverse multi-component melts from the previous experimental and theoretical studies. $Di_{64}An_{36}$, and BCR-2 refer to glasses in diopside-anorthite eutectic composition and Columbia River basalt glasses, respectively (see Table S3). The red diamonds (♦) refer to the normalized volume of $Di_{64}An_{36}$ melt estimated from acoustic wave velocity measurement (45). The pale red solid line refers to the normalized volume of $Di_{64}An_{36}$ melt obtained using first-principles simulations (67). Closed triangles (▲) and open triangles (△) refer to the normalized molar volume of BCR-2 glasses estimated from High pressure x-ray micro-tomography (HPXMT) and gigahertz- ultrasonic interferometry experiment in a DAC, respectively (44). The thick dotted line ('Clark I') is the original trend line for the data from HPXMT in the previous study (44). Thick solid line ('Clark II') is the modified trend line of the normalized volume of BCR-2 glasses. Closed squares (■), circles (●), and diamonds (♦) refer to the normalized volumes of diverse multi-component glasses estimated from refractive index measurement, such as alkali basaltic glass (68); tholeiite glass (69), and $Di_{64}An_{36}$ glass (70), respectively. The thin dotted line represents the trend line connecting the data for the tholeiite glass (69).

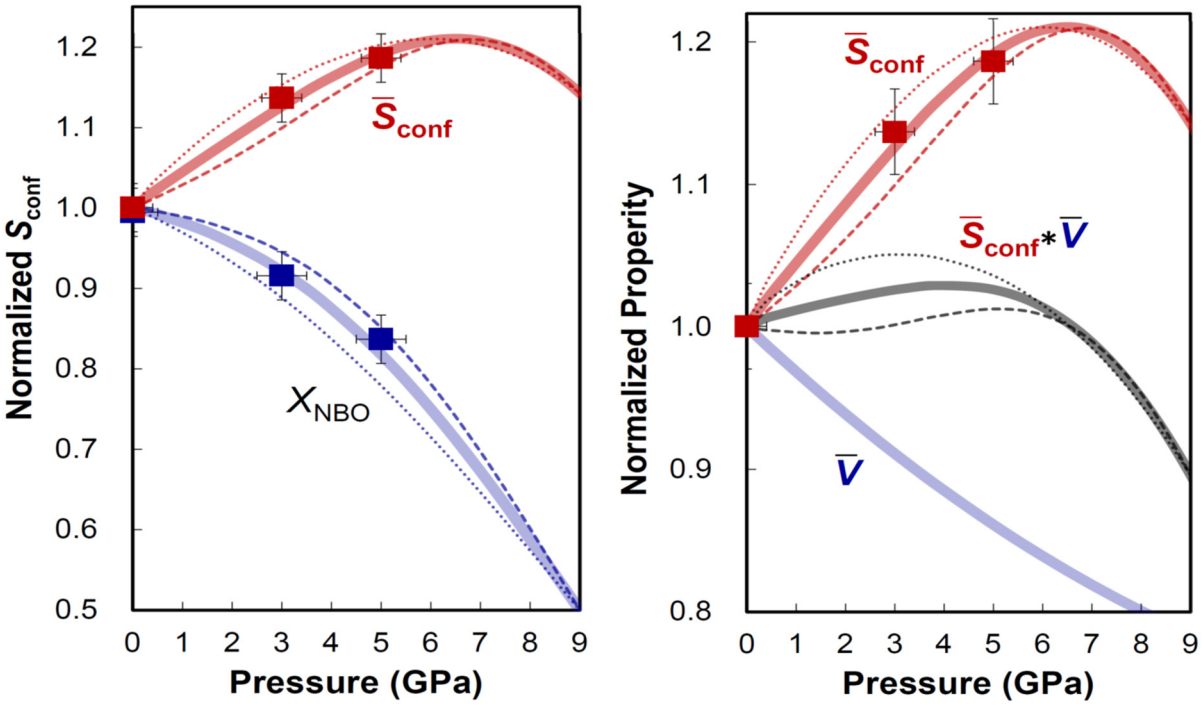

Figure S4 | Effect of pressure on the normalized configurational entropy. Left. Effect of pressure on the normalized configurational entropy ($\bar{S}_{conf}$, red square) of the $Di_{64}An_{36}$ glass. Variation in the normalized NBO fraction in model basaltic glass with pressure was also shown (X_{NBO}, blue square). The X_{NBO} beyond 5 GPa is modeled with Eq. S4 with $P_{XNBO=0.5}$ of 9 and β of 0.75. Variation in the normalized NBO fraction with varying β [from 0.62 (thick dashed line) to 1 (thin dashed line)] was also shown. A larger β often results in the X_{NBO} at 1 atm less than 1. In such a case, the X_{NBO} was renormalized to that at 1 atm. **Right.** Calculated $\bar{S}_{conf}*\bar{V}$ with varying β from 0.62 to 1.

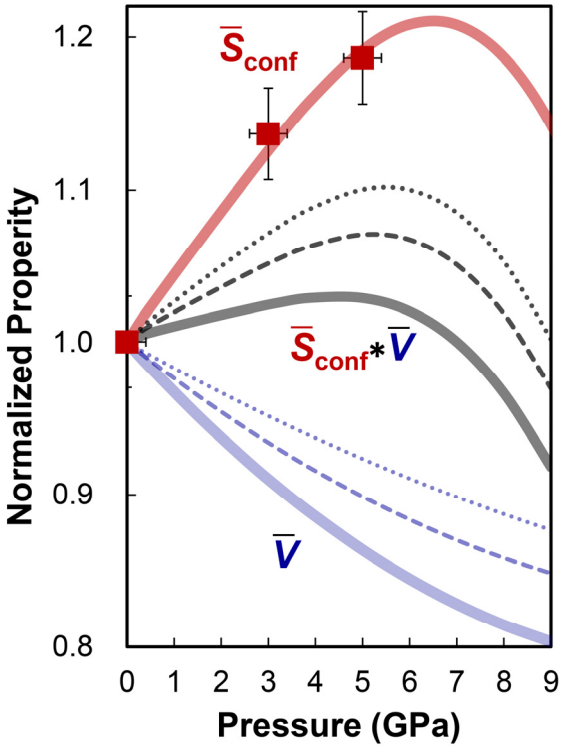

Figure S5 | Effect of pressure-induced decrease in normalized volume on $\overline{S}_{conf}$*$\overline{V}$. Variation in the normalized molar volume in basaltic glass with pressure was also shown (blue solid and dashed lines, see figure S3). A larger molar volume results in increase in $\overline{S}_{conf}$*$\overline{V}$ and vice versa.

SI References:

1. S. K. Lee, Simplicity in melt densification in multicomponent magmatic reservoris in Earth's interior revealed by multinuclear magnetic resonance. *Proc. Nat. Acad. Sci. U. S. A.* **108**, 6847-6852 (2011).
2. C. J. Benmore *et al.*, Structural and topological changes in silica glass at pressure. *Phys. Rev. B* **81**, 054105 (2010).
3. G. Shen, H. K. Mao, High-pressure studies with x-rays using diamond anvil cells. *Rep. Prog. Phys.* **80**, 016101 (2017).
4. R. J. Hemley, V. V. Struzhkin, R. E. Cohen, G. Shen, "Measuring high-pressure electronic and magnetic properties" in Treatise on Geophysics (Second Edition), G. Schubert, Ed. (Elsevier, Oxford, 2015), vol. 2, pp. 313-349.
5. Y. Kono *et al.*, Ultrahigh-pressure polyamorphism in GeO_2 glass with coordination number >6. *Proc. Nat. Acad. Sci. U. S. A.* **113**, 3436-3441 (2016).
6. Y. Kono, C. Park, C. Kenney-Benson, G. Shen, Y. Wang, Toward comprehensive studies of liquids at high pressures and high temperatures: Combined structure, elastic wave velocity, and viscosity measurements in the Paris–Edinburgh cell. *Phys. Earth Planet. Inter.* **228**, 269-280 (2014).
7. C. Prescher *et al.*, Beyond sixfold coordinated Si in SiO_2 glass at ultrahigh pressures. *Proc. Nat. Acad. Sci. U. S. A.* **114**, 10041-10046 (2017).
8. T. Sakamaki *et al.*, Ponded melt at the boundary between the lithosphere and asthenosphere. *Nat. Geosci.* **6**, 1041-1044 (2013).
9. G. Shen *et al.*, Effect of helium on structure and compression behavior of SiO_2 glass. *Proc. Nat. Acad. Sci. U. S. A.* **108**, 6004-6007 (2011).
10. G. Shen, Y. Wang, "High-pressure apparatus integrated with synchrotron radiation" in Reviews in Mineralogy and Geochemistry, G. S. Henderson, D. R. Neuville, R. T. Downs, Eds. (Mineralogical Society of America, 2014), vol. 78, pp. 745-777.
11. Y. Wang *et al.*, Atomistic insight into viscosity and density of silicate melts under pressure. *Nat. Commun.* **5**, 3241 (2014).
12. Y. Wang, G. Shen, High-pressure experimental studies on geo-liquids using synchrotron radiation at the Advanced Photon Source. *J. Earth Sci.* **25**, 939-958 (2014).
13. G. H. Wolf, P. F. McMillan, "Pressure effects on silicate melt structure and properties" in Structure, Dynamics, and Properties of Silicate Melts, J. F. Stebbins, P. F. McMillan, D. B. Dingwell, Eds. (Mineralogical Society of America, Washington, D.C., 1995), vol. 32, pp. 505-562.
14. A. Zeidler, P. S. Salmon, L. B. Skinner, Packing and the structural transformations in liquid and amorphous oxides from ambient to extreme conditions. *Proc. Nat. Acad. Sci. U. S. A.* **111**, 10045-10048 (2014).
15. A. Zeidler *et al.*, High-pressure transformation of SiO_2 glass from a tetrahedral to an octahedral network: A joint approach using neutron diffraction and molecular dynamics. *Phys. Rev. Lett.* **113**, 135501 (2014).
16. M. Guthrie *et al.*, Formation and structure of a dense octahedral glass. *Phys. Rev. Lett.* **93**, 115502 (2004).
17. T. Sato, N. Funamori, High-pressure structural transformation of SiO_2 glass up to 100 GPa. *Phys. Rev. B* **82**, 184102 (2010).
18. C. Sanloup *et al.*, Structural change in molten basalt at deep mantle conditions. *Nature*

503, 104-107 (2013).
19. V. Petkov, S. J. L. Billinge, S. D. Shastri, B. Himmel, Polyhedral units and network connectivity in calcium aluminosilicate glasses from high-energy x-ray diffraction. *Phys. Rev. Lett.* **85**, 3436-3439 (2000).
20. S. K. Lee, P. J. Eng, H. K. Mao, "Probing of pressure-Induced bonding transitions in crystalline and amorphous Earth materials: Insights from x-ray Raman scattering at high pressure" in Spectroscopic Methods in Mineralology and Materials Sciences, G. S. Henderson, D. R. Neuville, R. T. Downs, Eds. (Mineralogical Society of America, 2014), vol. 78, pp. 139-174.
21. J. R. Allwardt *et al.*, Aluminum coordination and the densification of high-pressure aluminosilicate glasses *Am. Mineral.* **90**, 1218-1222 (2005).
22. S. K. Lee, Effect of pressure on structure of oxide glasses at high pressure: Insights from solid-state NMR of quadrupolar nuclides. *Solid State Nucl. Magn. Reson.* **38**, 45-57 (2010).
23. S. K. Lee *et al.*, Effect of network polymerization on the pressure-induced structural changes in sodium aluminosilicate glasses and melts: ^{27}Al and ^{17}O solid-state NMR study. *J. Phys. Chem. C* **116**, 2183-2191 (2012).
24. J. F. Stebbins, Glass structure, melt structure, and dynamics: Some concepts for petrology. *Am. Mineral.* **101**, 753-768 (2016).
25. J. F. Stebbins, X. Y. Xue, "NMR spectroscopy of inorganic Earth materials" in Spectroscopic Methods in Mineralogy and Materials Sciences, G. S. Henderson, D. R. Neuville, R. T. Downs, Eds. (Mineralogical Society of America, 2014), vol. 78, pp. 605-653.
26. S. Bista, J. F. Stebbins, W. B. Hankins, T. W. Sisson, Aluminosilicate melts and glasses at 1 to 3 GPa: Temperature and pressure effects on recovered structural and density changes. *Am. Mineral.* **100**, 2298-2307 (2015).
27. S. Bista, J. F. Stebbins, J. Wu, T. M. Gross, Structural changes in calcium aluminoborosilicate glasses recovered from pressures of 1.5 to 3 GPa: Interactions of two network species with coordination number increases. *J. Non-Cryst. Solids* **478**, 50-57 (2017).
28. S. Y. Park, S. K. Lee, Structure and disorder in basaltic glasses and melts: Insights from high-resolution solid-state NMR study of glasses in diopside–Ca-tschermakite join and diopside–anorthite eutectic composition. *Geochim. Cosmochim. Acta* **80**, 125-142 (2012).
29. S. Y. Park, S. K. Lee, Probing the structure of Fe-free model basaltic glasses: A view from a solid-state ^{27}Al and ^{17}O NMR study of Na-Mg silicate glasses, Na_2O-MgO-Al_2O_3-SiO_2 glasses, and synthetic Fe-free KLB-1 basaltic glasses. *Geochim. Cosmochim. Acta* **238**, 563-579 (2018).
30. S. K. Lee *et al.*, Structure of shock compressed model basaltic glass: Insights from O K-edge X-ray Raman scattering and high-resolution ^{27}Al NMR spectroscopy. *Geophys. Res. Lett.* **39**, L05306 (2012).
31. S. K. Lee, H.-I. Kim, E. J. Kim, K. Y. Mun, S. Ryu, Extent of disorder in magnesium aluminosilicate glasses: Insights from ^{27}Al and ^{17}O NMR. *J. Phys. Chem. C* **120**, 737-749 (2016).
32. H.-I. Kim, J. C. Sur, S. K. Lee, Effect of iron content on the structure and disorder of iron-bearing sodium silicate glasses: A high-resolution ^{29}Si and ^{17}O solid-state NMR study. *Geochim. Cosmochim. Acta* **173**, 160-180 (2016).
33. K. Hirose, I. Kushiro, Partial melting of dry peridotites at high pressures: determination

of compositions of melts segregated from peridotite using aggregates of diamond. *Earth Planet. Sci. Lett.* **114**, 477-489 (1993).
34. E. Cottrell, K. A. Kelley, The oxidation state of Fe in MORB glasses and the oxygen fugacity of the upper mantle. *Earth Planet. Sci. Lett.* **305**, 270-282 (2011).
35. S. R. Elliot, *Physics of Amorphous Materials* (Wiely-Blackwell, 2016).
36. X. Xue, M. Kanzaki, R. G. Trønnes, J. F. Stebbins, Silicon coordination and speciation changes in a silicate liquid at high pressures. *Science* **245**, 962-964 (1989).
37. X. Xue, J. F. Stebbins, M. Kanzaki, P. F. McMillan, B. Poe, Pressure-induced silicon coordination and tetrahedral structural changes in alkali oxide-silica melts up to 12 GPa: NMR, Raman, and infrared spectroscopy. *Am. Mineral.* **76**, 8-26 (1991).
38. B. B. Karki, D. Bhattarai, L. Stixrude, First-principles simulations of liquid silica: Structural and dynamical behavior at high pressure. *Phys. Rev. B* **76**, 104205 (2007).
39. L. Stixrude, B. Karki, Structure and freezing of $MgSiO_3$ liquid in Earth's lower mantle. *Science* **310**, 297-299 (2005).
40. S. K. Lee, H. I. Kim, E. J. Kim, K. Y. Mun, S. Ryu, Extent of disorder in magnesium aluminosilicate glasses: Insights from Al-27 and O-17 NMR. *J. Phys. Chem. C* **120**, 737-749 (2016).
41. S. K. Lee *et al.*, Effect of network polymerization on the pressure-induced structural changes in sodium aluminosilicate glasses and melts: Al-27 and O-17 solid-state NMR study. *J. Phys. Chem. C* **116**, 2183-2191 (2012).
42. S. K. Lee, P. J. Eng, H. K. Mao, J. F. Shu, Probing and modeling of pressure-induced coordination transformation in borate glasses: Inelastic x-ray scattering study at high pressure. *Phys. Rev. B* **78**, 214203 (2008).
43. S. K. Lee *et al.*, Degree of permanent densification in oxide glasses upon extreme compression up to 24 GPa at room temperature. *J. Phys. Chem. Lett.* **11**, 2917-2924 (2020).
44. A. N. Clark, C. E. Lesher, S. D. Jacobsen, Y. Wang, Anomalous density and elastic properties of basalt at high pressure: Reevaluating of the effect of melt fraction on seismic velocity in the Earth's crust and upper mantle. *J. Geophys. Res. Solid Earth* **121**, 4232-4248 (2016).
45. Y. Ai, R. A. Lange, New acoustic velocity measurements on CaO-MgO-Al_2O_3-SiO_2 liquids: Reevaluation of the volume and compressibility of $CaMgSi_2O_6$-$CaAl_2Si_2O_8$ liquids to 25 GPa. *J. Geophys. Res. Solid Earth* **113**, B04203 (2008).
46. S. Sugai, H. Sotokawa, D. Kyokane, A. Onodera, Bose peak in the Raman spectra of densified SiO_2 and GeO_2 glass under high pressure. *Physica B: Condensed Matter* **219**, 293-295 (1996).
47. S. K. Lee, S. Ryu, Probing of triply coordinated oxygen in amorphous Al_2O_3. *J. Phys. Chem. Lett.* **9**, 150-156 (2018).
48. A. K. Verma, P. Modak, B. B. Karki, First-principles simulations of thermodynamical and structural properties of liquid Al_2O_3 under pressure. *Physical Review B* **84**, 174116 (2011).
49. D. B. Ghosh, B. B. Karki, L. Stixrude, First-principles molecular dynamics simulations of $MgSiO_3$ glass: Structure, density, and elasticity at high pressure. *Am. Mineral.* **99**, 1304-1314 (2014).
50. Y. H. Kim *et al.*, Structural transitions in $MgSiO_3$ glasses and melts at the core-mantle boundary observed via inelastic X-ray scattering. *Geophys. Res. Lett.* **46**, 13756-13764 (2019).

51. J. F. Stebbins, Temperature effects on the network structure of oxide melts and their consequences for configurational heat capacity. *Chem. Geol.* **256**, 80-91 (2008).
52. A. N. Clark, C. E. Lesher, Elastic properties of silicate melts: Implications for low velocity zones at the lithosphere-asthenosphere boundary. *Sci. Adv.* **3**, 1701312 (2017).
53. J. Liu, J. F. Lin, Abnormal acoustic wave velocities in basaltic and (Fe, Al)-bearing silicate glasses at high pressures. *Geophys. Res. Lett.* **41**, 8832-8839 (2014).
54. B. Mantisi, A. Tanguy, G. Kermouche, E. Barthel, Atomistic response of a model silica glass under shear and pressure. *Eur. Phys. J. B* **85**, 304 (2012).
55. Y. Wang *et al.*, Atomistic insight into viscosity and density of silicate melts under pressure. *Nature Commun.* **5**, 1-10 (2014).
56. S. K. Lee, Simplicity in melt densification in multicomponent magmatic reservoirs in Earth's interior revealed by multinuclear magnetic resonance. *Proc. Nat. Acad. Sci. U. S. A.* **108**, 6847-6852 (2011).
57. S. K. Lee, G. D. Cody, Y. Fei, B. O. Mysen, Nature of polymerization and properties of silicate melts and glasses at high pressure. *Geochim. Cosmochim. Acta* **68**, 4189-4200 (2004).
58. B. T. Poe *et al.*, Silicon and oxygen self-diffusivities in silicate liquids measured to 15 gigapascals and 2800 Kelvin. *Science* **276**, 1245-1248 (1997).
59. J. L. Yarger *et al.*, Al coordination changes in high-pressure aluminosilicate liquids. *Science* **270**, 1964-1967 (1995).
60. C. E. Lesher, "Self-diffusion in silicate Melts: Theory, observations and applications to magmatic systems" in Reviews in Mineralogy and Geochemistry, Y. Zhang, D. Cherniak, Eds. (Mineralogical Society of America, Washington, DC, 2010), vol. 72, chap. 7, pp. 269-309.
61. B. O. Mysen, Element partitioning between minerals and melt, melt composition, and melt structure. *Chem. Geol.* **213**, 1-16 (2004).
62. W. M. White, *Geochemistry* (Wiley-Blackwell, 2013).
63. D. M. Miller, S. L. Goldstein, C. H. Langmuir, Cerium lead and lead-isotope ratios in arc magmas and the enrichment of lead in the continents. *Nature* **368**, 514-520 (1994).
64. K. Hirose, Y. Fei, Subsolidus and melting phase relations of basaltic composition in the uppermostlower mantle. *Geochim. Cosmochim. Acta* **66**, 2099-2108 (2002).
65. S. J. Gaudio, C. E. Lesher, H. Maekawa, S. Sen, Linking high-pressure structure and density of albite liquid near the glass transition. *Geochim. Cosmochim. Acta* **157**, 28-38 (2015).
66. S. Bista, J. F. Stebbins, The role of modifier cations in network cation coordination increases with pressure in aluminosilicate glasses and melts from 1 to 3 GPa. *Am. Mineral.* **102**, 1657-1666 (2017).
67. S. Bajgain, D. B. Ghosh, B. B. Karki, Structure and density of basaltic melts at mantle conditions from first-principles simulations. *Nature Commun.* **6**, 1-7 (2015).
68. R. G. Kuryaeva, Effect of high pressure on the refractive index and density of natural aluminosilicate glasses of alkali basalt composition in the SiO_2-Al_2O_3-TiO_2-Fe_2O_3-P_2O_5-FeO-MnO-CaO-MgO-Na_2O-K_2O system. *Glass Phys. Chem.* **30**, 523-531 (2004).
69. R. G. Kuryaeva, V. A. Kirkinskii, Influence of high pressure on the refractive index and density of tholeiite basalt glass. *Phys. Chem. Miner.* **25**, 48-54 (1997).
70. R. G. Kuryaeva, N. V. Surkov, Refractive index and compressibility of $Di_{64}An_{36}$ glass over a pressure range of 0–5.0 GPa. *Geochem. Int.* **50**, 1026-1031 (2012).